Biointerface Research in Applied Chemistry
Open-Access Journal (ISSN: 2069-5837)

Article
Volume 15, Issue 4, 2025, 55
https://doi.org/10.33263/BRIAC154.055

Smart Nanomaterials and Sustainable Energy Sources: Evaluation of Metal Doping Effect on Gallium Nitride Nanocages to Increase the Energy Storage using a First-Principles Study

Fatemeh Mollaamin [1,*]

[1] Department of Biomedical Engineering, Faculty of Engineering and Architecture, Kastamonu University, Kastamonu, Turkey
* Correspondence: fmollaamin@kastamonu.edu.tr;

Received: 1.11.2024; Accepted: 19.07.2025; Published: 9.08.2025

Abstract: The growth of an efficient yet durable photoelectrode is of paramount importance for the deployment of solar-fuel production. The notable fragile signal intensity close to the parallel edge of the nanocluster sample might be owing to manganese binding, induced non-spherical distribution of GaMnN, AlGaMnN, or InGaMnN heteroclusters. Manganese builds in as an acceptor in place of Ga and forms a simple complex with N. A comprehensive investigation on hydrogen grabbing by heteroclusters of Mn-doped GaN, AlGaN, InGaN was carried out via DFT computations at the CAM–B3LYP–D3/6–311+G (d,p) level of theory. A vaster jointed area engaged by an isosurface map for Mn-doped GaN, AlGaN, InGaN, towards formation of nanocomposites of GaMnN-H, AlGaMnN-H, InGaMnN-H after hydrogen adsorption due to labeling atoms of N(4), Mn(5), H(18), respectively. Therefore, it can be considered that manganese in the functionalized GaMnN, AlGaMnN, or InGaMnN might have more impressive sensitivity for accepting electrons in the process of hydrogen adsorption. Furthermore, GaMnN, AlGaMnN, or InGaMnN are potentially advantageous for certain high-frequency applications requiring batteries for energy storage. The advantages of manganese over GaN, AlGaN, or InGaN include its higher electron and hole mobility, allowing manganese-doped devices to operate at higher frequencies than non-doped devices. This research article demonstrates that gallium nitride alloys lead to sustained operation and enhanced catalytic activity, thus showing promise as protective catalytic coatings for hydrogen adsorption.

Keywords: electronic structure; metal doping; batteries; hydrogen adsorption; energy storage; aluminum gallium nitride; indium gallium nitride; first-principles study; DFT.

1. Introduction

A binary III/V direct bandgap semiconductor called Gallium nitride (GaN) is a very hard material with a wide bandgap applied in a variety of technologies, including optoelectronic, high-power electronics, and light-emitting diodes, partly due to its favorable thermal properties [1–5].

The nitrides of group III in the periodic table have low sensitivity to ionizing radiation, which makes them appropriate materials for solar cell arrays for satellites. Therefore, space

applications could also benefit as devices have shown stability in high radiation environments [6–8].

Ternary "AlGaN" alloys have been recognized as promising materials for realizing deep ultraviolet (DUV) optoelectronic devices with operating wavelengths down to 200 nm [9]. For the development of high-performance AlGaN-based "DUV" devices, high-conductivity p-type Al-rich $Al_xGa_{1-x}N$ ($x \geq 0.4$) is essential. Many studies have shown that enhancing the p-type conductivity has a significant effect on improving both the electrical and optical properties of AlGaN DUV optoelectronics [10–16].

The researchers have estimated the suitability of Mn-doped $In_{1-x}Ga_xN$ as an IB material. They predicted that the $In_{1-x}Ga_xN$-based solar cells with an Mn-doped absorption layer could achieve maximum efficiency [17].

The ternary semiconductor of Indium gallium nitride (InGaN) as solar cells is remarkable owing to the adjustable direct band gap energy of InGaN, veiling the total solar spectrum arraying from 0.7 to 3.4 eV [18,19], as well as preferable photovoltaic specifics of InGaN consisting of vast absorption coefficients [20] and high carrier mobility. Furthermore, great fixity and excellent radiation persistence of InGaN alloys permit the function of InGaN-based instruments in the utmost situations, such as space and geocentric usages [18, 21]. The solar cells of InGaN were constructed with low indium amounts of the InGaN alloy compounds [22–24], which conduces to an enhancement in the band gap energy of InGaN and then eventuates in the absorption of shorter wavelengths of solar radiation. Therefore, to find out InGaN solar cells with high yield, the In amount in the InGaN active layer of these solar cells should be enhanced to compensate for a large part of the solar spectrum [25–31]. Recently, it has been suggested that the application of dual nanogratings of Si and other organic solar cells, which are mostly in direct contact with the active area of the solar cells [32–37].

Recently, researchers have proposed an InGaN/GaN p-i-n thin-film solar cell that includes a dual nanograting compound: silver nanogratings on the back of the solar cell and GaN-NGs on the front [38].

In this paper, we propose the feasible semiconductors of GaN, AlGaN, and InGaN, which are doped with manganese. We carried out molecular modelling considering the geometrical parameters of doping atoms on the surface of GaMnN, AlGaMnN, and InGaMnN through hydrogen absorption status, and the current charge density of the batteries was studied. Moreover, the effect of a relative chemical shift between GaN, AlGaN, InGaN, and doped heteroclusters of the batteries was also investigated.

2. Materials and Methods

Manganese-doped gallium nitride is theoretically expected to be a diluted magnetic semiconductor at room temperature. The Mn-doped GaN, AlGaN, and InGaN nanocomposites were calculated within the framework of first-principles calculation based on density functional theory (DFT) (Figure 1a,b,c). The rigid potential energy surface via density functional theory [39–52] was performed using the Gaussian 16 revision C.01 program package [53] and GaussView 6.1 [54]. The coordination input for energy storage on the batteries has applied 6–311+G (d,p) and EPR–3 basis sets.

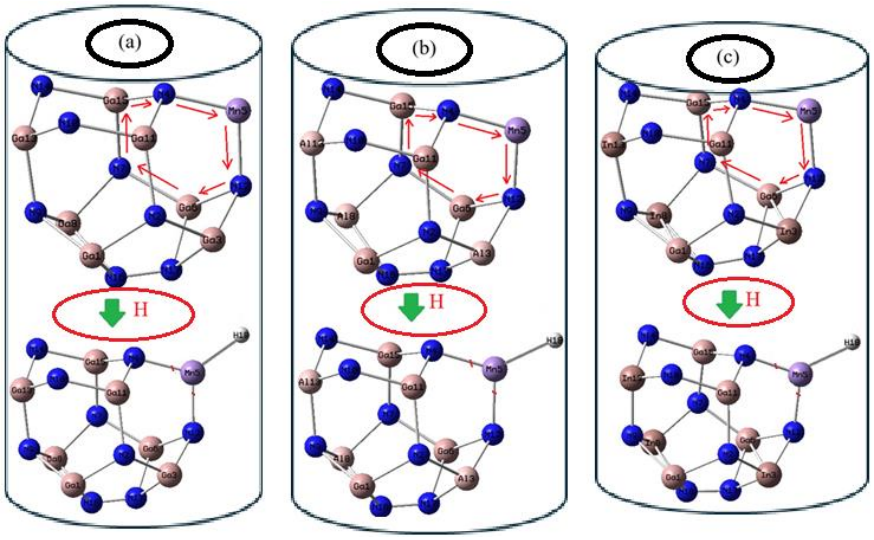

Figure 1. Characterization of heteroclusters includes **(a)** GaMnN/GaMnN–H; **(b)** AlGaMnN/AlGaMnN –H; **(c)** InGaMnN/InGaMnN–H through a labeled ring in a clockwise manner, including Mn5, N12, Ga6, N7, Ga15, N4 towards H-adsorption.

First, we optimized the structural parameters of nanoclusters of GaN, AlGaN, and InGaN, which are doped with manganese, towards the formation of heteroclusters of GaMnN, AlGaMnN, and InGaMnN for obtaining the highest short-circuit current density. Then, Figure 1 shows the process of hydrogen adsorption on heteroclusters of GaMnN, AlGaMnN, and InGaMnN, which are varied to maximize the absorption in the active region. Manganese builds in as an acceptor in place of Ga and forms a simple complex with N. This is a utility used to calculate ring area and perimeter, since ring area is sometimes involved in wavefunction analysis. In this function, it is needed to input the index of the atoms in the ring in a clockwise manner, including Mn5, N12, Ga6, N7, Ga15, N4 (Figure 1a,b,c). Then, the total ring area and total ring perimeter for a tailored ring are 9.6981 Å and 11.6921 $Å^2$, respectively (Figure 1a,b,c).

Dispersion effects included via semiempirical atom-pairwise interactions via the DFT-D2 or DFT-D3 methods have been shown to give quite accurate thermochemistry for both covalently bonded systems and systems dominated by dispersion forces [55–60].

3. Results and Discussion

In this article, the efficiency of metal-doped hybrid nanoalloys of GaMnN, AlGaMnN, InGaMnN, and their hydrated complexes of GaMnN–H, AlGaMnN–H, InGaMnN–H, for energy-saving in batteries.

3.1. Theory of Nuclear Quadrupole Resonance (NQR).

The NQR frequencies have been measured for GaMnN, AlGaMnN, and InGaMnN towards estimating the hydrated nanocluster of GaMnN-H, AlGaMnN-H, and InGaMnN-H (Table 1). The NQR method is related to the multipole expansion in Cartesian coordinates as in equation (1) [61,62].

$$V(r) = V(0) + \left[\left(\frac{\partial V}{\partial x_i}\right)\Big|_0 . x_i\right] + \frac{1}{2}\left[\left(\frac{\partial^2 V}{\partial x_i x_j}\right)\Big|_0 . x_i x_j\right] \quad (1)$$

After that, a simplification of the equation (6), there are only the second derivatives related to the identical variable for the potential energy [61–64]:

$$U = -\frac{1}{2}\int_{\mathcal{D}} d^3\, r\, \rho_r \left[\left(\frac{\partial^2 V}{\partial x_i^2}\right)\Big|_0 . x_i^2\right] = -\frac{1}{2}\int_{\mathcal{D}} d^3\, r\, \rho_r \left[\left(\frac{\partial E_i}{\partial x_i}\right)\Big|_0 . x_i^2\right]$$
$$= -\frac{1}{2}\left(\frac{\partial E_i}{\partial x_i}\right)\Big|_0 . \int_{\mathcal{D}} d^3\, r\, [\rho(r) . x_i^2] \quad (2)$$

The "electric potential" through carrying over the electric charge was measured for GaMnN/GaMnN-H, AlGaMnN/AlGaMnN-H, and InGaMnN/InGaMnN-H complexes (Table 1). Mn, Al, Ga, In, N, and the hydrogen atom absorbed on GaMnN, AlGaMnN, and InGaMnN have been calculated through the "Bader charge" and electronic potential properties. The values detect that by augmenting the negative charge of various atoms, the electric potential extracted from "NQR" calculations grows. Besides, the elements of N2, N4, N7, N9, N10, N12, N14 of GaMnN, AlGaMnN, InGaMnN have exhibited the most efficiency for admitting the electron from the "electron donor" of H18 adsorbed on GaMnN, AlGaMnN, InGaMnN (Table 1).

Table 1. The electric potential (E_p/a.u.) and Bader charge (Q/coulomb) through NQR calculation for selected atoms of GaMnN, GaMnN-H, AlGaMnN, AlGaMnN-H, InGaMnN, and InGaMnN-H heteroclusters.

GaMnN			GaMnN–H			AlGaMnN		
Atom	**Q**	**E_p**	**Atom**	**Q**	**E_p**	**Atom**	**Q**	**E_p**
Ga1	0.9961	–1.2490	Ga1	1.0084	–1.2238	Ga1	0.9852	–1.2503
N2	–1.0483	–18.408	N2	–1.0386	–18.391	N2	–1.1478	–18.4129
Ga3	0.9744	–1.2497	Ga3	0.9936	–1.2285	Al3	1.2520	–1.2192
N4	–1.0171	–18.4093	N4	–0.9210	–18.3993	N4	–1.0561	–18.4182
Mn5	0.7522	–16.6505	Mn5	0.4224	–16.6378	Mn5	0.7651	–16.6575
Ga6	0.9743	–1.2497	Ga6	0.9933	–1.2267	Ga6	0.9729	–1.2503
N7	–1.0482	–18.4083	N7	–1.0490	–18.3864	N7	–1.1444	–18.4122
Ga8	0.9958	–1.2490	Ga8	1.0123	–1.2224	Al8	1.2493	–1.2188
N9	–1.0455	–18.4122	N9	–1.0148	–18.3901	N9	–1.2161	–18.4192
N10	–0.6809	–18.4169	N10	–0.6763	–18.3855	N10	–0.7651	-18.4241
Ga11	1.0012	–1.2522	Ga11	1.0242	–1.2392	Ga11	0.9972	-1.2552
N12	–0.9800	–18.4081	N12	–0.9025	–18.3842	N12	–1.0750	-18.4156
Ga13	0.9259	–1.2537	Ga13	0.9193	–1.2418	Al13	1.2071	-1.2257
N14	–0.6808	–18.4169	N14	–0.6916	–18.3896	N14	–0.7669	-18.4229
Ga15	1.0012	–1.2522	Ga15	1.0272	–1.2358	Ga15	1.0015	-1.2544
N16	–0.5692	–18.3631	N16	–0.5456	–18.3231	N16	–0.6368	-18.3667
N17	–0.5512	–18.3641	N17	–0.5327	–18.3222	N17	–0.6220	-18.3673
-	-	-	H18	–0.0285	–1.1338	-	-	-
AlGaMnN-H			**InGaMnN**			**InGaMnN-H**		
Atom	**Q**	**E_p**	**Atom**	**Q**	**E_p**	**Atom**	**Q**	**E_p**
Ga1	0.9958	–1.2238	Ga1	0.9511	–1.2550	Ga1	1.3172	–1.2338
N2	–1.1288	–18.391	N2	–1.0594	–18.4264	N2	–1.4501	–18.3901
Al3	1.2506	–1.2285	In3	1.0827	–1.1292	In3	1.4791	–1.1137
N4	–0.9446	–18.3993	N4	–1.0219	–18.4176	N4	–1.3388	–18.3983
Mn5	0.3908	–16.6378	Mn5	0.7195	–16.6614	Mn5	0.8126	–16.4568
Ga6	0.9814	–1.2267	Ga6	0.9420	–1.2549	Ga6	1.2959	–1.2328
N7	–1.1129	–18.3864	N7	–1.0627	–18.4247	N7	–1.4452	–18.3922
Al8	1.2696	–1.2224	In8	1.0981	–1.1280	In8	1.5085	–1.1173
N9	–1.1616	–18.3901	N9	–1.0715	–18.4421	N9	–1.4269	–18.4351
N10	–0.7699	–18.3855	N10	–0.7066	–18.4367	N10	–0.8648	–18.3712
Ga11	1.0024	–1.2392	Ga11	0.9750	–1.2612	Ga11	1.4177	–1.2144
N12	–0.9475	–18.3842	N12	–0.9944	–18.4280	N12	–1.3611	–18.413
Al13	1.1771	–1.2418	In13	1.0188	–1.1362	In13	1.3032	–1.1244
N14	–0.7570	–18.3896	N14	–0.711	–18.4339	N14	–0.9195	–18.3859
Ga15	1.0088	–1.2358	Ga15	0.9812	–1.2596	Ga15	1.4087	–1.2201
N16	–0.6195	–18.3231	N16	–0.5787	–18.3801	N16	–0.8417	–18.422
N17	–0.6003	–18.3222	N17	–0.5623	–18.3807	N17	–0.8212	–18.4186
H18	–0.0345	–1.1338	-	-	-	H18	–0.0735	–1.1254

In Figure 2 (a,b,c), the electric potential versus Bader charge for Mn, Al, Ga, In, N, and the hydrogen atom absorbed on GaMnN, AlGaMnN, and InGaMnN. Therefore, the behavior of Mn, Ga, and N atoms in GaMnN with high sensitivity based on the relation coefficient of R^2_{GaMnN}

= 0.9095; however, hydrogen adsorption on the GaMnN (GaMnN-H) has shown high sensitivity with a relation coefficient of $R^2_{GaMnN-H}$ = 0.9897. In Figure 2(b), the behavior of Mn, Al, Ga, and N atoms in AlGaMnN and hydrogen adsorption on the AlGaMnN and formation of AlGaMnN-H with high sensitivity of $R^2_{AlGaMnN}$ = 0.8974 and $R^2_{AlGaMnN-H}$ = 0.9548, respectively.

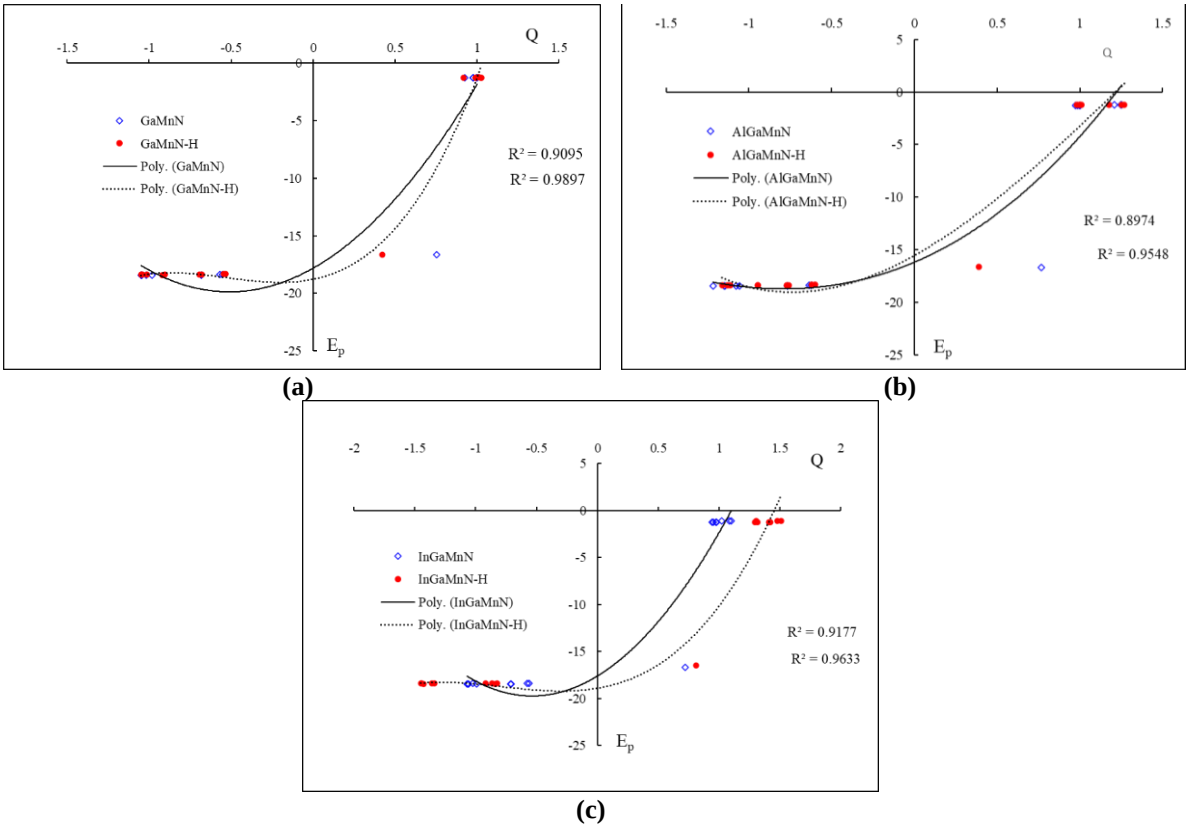

Figure 2. "Electric potential" (E_p/a.u.) versus "Bader charge" (Q/coulomb) through "NQR" calculation for **(a)** GaMnN/GaMnN-H; **(b)** AlGaMnN/AlGaMnN-H; **(c)** InGaMnN/InGaMnN-H nanoclusters.

The fluctuated peaks for electric potential have been shown around hydrogen adsorption on the InGaMnN, which demonstrates the electron accepting specifications of hydrogen versus the Mn, In, Ga, N of InGaMnN and InGaMnN-H (Figure 2c). Based on the mentioned results, there can be renewed interest in the combination of manganese, aluminum, gallium, and indium in the nanoclusters of GaMnN, AlGaMnN, and InGaMnN for potential applications in next-generation electronic devices.

3.2. Analysis of nuclear magnetic resonance spectra.

Based on the resulting amounts, nuclear magnetic resonance (NMR) spectra of GaMnN, AlGaMnN, and InGaMnN heteroclusters as the potential molecules for energy storage can unravel the efficiency of these complexes in batteries through hydrogen adsorption. From the DFT calculations, the chemical shielding (CS) tensors in the principal axes system to estimate the isotropic chemical-shielding (CSI) and anisotropic chemical-shielding (CSA) [65]:

$$\sigma_{iso} = (\sigma_{11} + \sigma_{22} + \sigma_{33})/3 \quad (3)$$

$$\sigma_{aniso} = \sigma_{33} - (\sigma_{22} + \sigma_{11})/2 \quad (4)$$

The NMR data of isotropic (σ_{iso}) and anisotropic shielding tensors (σ_{aniso}) for Mn-doped GaN, AlGaN, and InGaN and their hydrated derivatives of GaMnN-H, AlGaMnN-H, and

InGaMnN-H have been computed by the Gaussian 16 revision C.01 program package [53] and are shown in Table 2.

Table 2. Data of NMR shielding tensors (ppm) for selected atoms of GaMnN, GaMnN-H, AlGaMnN, AlGaMnN-H, InGaMnN, and InGaMnN-H heteroclusters.

GaMnN			GaMnN-H			AlGaMnN		
Atom	**σ_{iso}**	**σ_{aniso}**	**Atom**	**σ_{iso}**	**σ_{aniso}**	**Atom**	**σ_{iso}**	**σ_{aniso}**
Ga1	10.6772	8.1116	Ga1	7.8121	31.2686	Ga1	10.4656	8.1593
N2	127.8331	150.7727	N2	11.3237	302.2757	N2	146.5709	121.3465
Ga3	8.8962	7.1266	Ga3	0.0389	103.9122	Al3	7.3554	7.0508
N4	59.2200	255.8445	N4	518.4328	1015.7500	N4	89.0872	176.7298
Mn5	1103.1944	682.7562	Mn5	61898.6207	83180.6883	Mn5	860.1968	607.8757
Ga6	8.9005	7.1468	Ga6	2.0906	109.3062	Ga6	8.7556	6.9697
N7	128.1480	149.7778	N7	45.0158	440.5489	N7	146.5804	115.6052
Ga8	10.6774	8.0754	Ga8	5.6210	31.7011	Al8	9.1447	9.2445
N9	41.8262	220.7655	N9	445.6927	929.9371	N9	97.5588	202.5538
N10	1008.9373	1461.3802	N10	3715.8543	8298.3128	N10	1048.8518	1558.0300
Ga11	4.0487	15.5383	Ga11	0.2483	102.0391	Ga11	3.0958	15.6767
N12	120.7217	362.2518	N12	367.1035	1288.8994	N12	94.3074	348.4218
Ga13	2.2765	25.1952	Ga13	35.1872	123.5145	Al13	4.1183	27.4952
N14	1007.7725	1458.0491	N14	1857.1102	7832.5114	N14	1063.7258	1561.8895
Ga15	4.0563	15.5221	Ga15	11.5119	73.3284	Ga15	3.0675	15.6962
N16	120.6766	305.8095	N16	655.7327	1345.8956	N16	119.1640	317.7316
N17	180.8583	320.6671	N17	1055.9230	1712.1127	N17	171.0876	325.8904
-	-	-	H18	40.6176	502.4079	-	-	-
AlGaMnN-H			**InGaMnN**			**InGaMnN-H**		
Atom	**σ_{iso}**	**σ_{aniso}**	**Atom**	**σ_{iso}**	**σ_{aniso}**	**Atom**	**σ_{iso}**	**σ_{aniso}**
Ga1	9.4127	57.4573	Ga1	9.8561	9.0718	Ga1	1.6742	42.3400
N2	523.2930	1969.3799	N2	141.2874	139.242	N2	43.0241	535.2459
Al3	3.9293	125.8000	In3	10.6228	6.0792	In3	16.1328	137.0235
N4	1362.4308	2433.1374	N4	70.7476	185.3866	N4	1588.0044	3484.4781
Mn5	44890.8709	68750.2634	Mn5	1100.8028	655.478	Mn5	75829.2468	87460.2786
Ga6	14.4225	140.9499	Ga6	8.0587	6.4922	Ga6	12.6556	135.7235
N7	367.1748	1905.4354	N7	138.2746	141.262	N7	190.1028	374.0311
Al8	1.3642	33.6753	In8	11.5107	8.9599	In8	3.9630	42.2998
N9	1645.6588	2817.2566	N9	76.7525	215.6169	N9	105.9158	687.9281
N10	2093.5030	9430.3119	N10	1078.6734	1612.3978	N10	6052.6589	10061.7128
Ga11	33.2386	113.4686	Ga11	2.4981	16.2989	Ga11	52.0566	69.7265
N12	610.2133	1774.9398	N12	101.3662	375.9026	N12	883.0356	2354.1239
Al13	10.8519	248.5418	In13	0.6973	25.46	In13	17.9037	85.9004
N14	3210.8323	7998.7947	N14	1134.3858	1669.9935	N14	11759.9230	18294.7406
Ga15	26.8216	118.0277	Ga15	1.9593	16.6879	Ga15	87.7874	114.0007
N16	336.4981	1962.7560	N16	129.6965	346.1977	N16	123.9797	695.5940
N17	498.3192	5128.1686	N17	189.0956	365.8149	N17	216.7121	726.1410
H18	26.2759	347.0249	-	-	-	H18	91.2315	651.1319

The notable fragile signal intensity close to the parallel edge of the nanocluster sample might be owing to manganese binding, induced non-spherical distribution of GaN (Figure 3a) and AlGaMnN (Figure 3b) heteroclusters. Figure 3c exhibited the same tendency of shielding; however, a considerable deviation exists from the doping atoms of manganese as electron acceptors on the surface of the InGaMnN heterocluster.

The observed increase in the chemical shift anisotropies spans for nanocages of GaMnN/GaMnN-H (Figure 3a) and InGaMnN/InGaMnN-H (Figure 3c) is near N10 and N14, and for AlGaMnN /AlGaMnN-H is close to N10, N14, and N17 (Figure 3b). The yield of electromagnetic shifting can be directed by the mentioned active nitrogen atoms extracted from hybrid nanomaterials. So, it can be observed that doped heteroclusters of GaMnN, AlGaMnN, or InGaMnN might ameliorate the capability of GaN-based nanocomposites in batteries for energy storage.

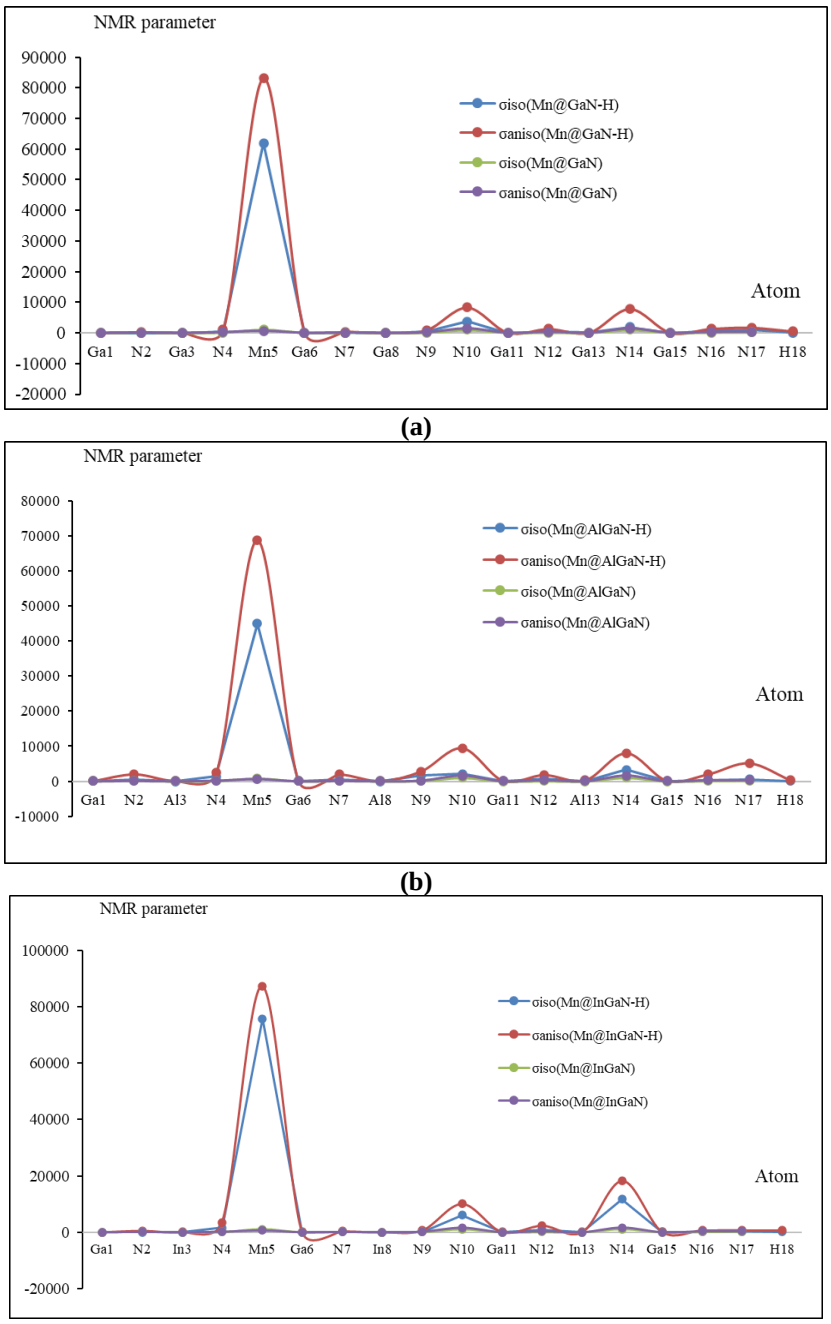

Figure 3. The NMR spectra for heteroclusters of **(a)** GaMnN / GaMnN –H; **(b)** AlGaMnN / AlGaMnN –H; **(c)** InGaMnN/ InGaMnN –H.

3.3. Insight into infrared spectroscopy and thermochemistry.

The infrared spectroscopy (IR) has been performed for nanocomposites of GaMnN/GaMnN-H (Figure 4a, a′), AlGaMnN/AlGaMnN-H (Figure 4b, b′), and InGaMnN/InGaMnN-H (Figure 4c, c′) through hydrogen adsorption.

The frequency value through the IR curves between 200–1000 cm^{-1} for GaMnN with one sharp peak around 414.78 cm^{-1} (Figure 4a) has been shifted to two pointed peaks around 863.78 and 921.24 cm^{-1} of GaMnN-H (Figure 4a′). However, Figure 4(b) shows two sharp peaks around 389.02 and 713.88 cm^{-1} for AlGaMnN that have been shifted to one sharp peak around 952.45 cm^{-1} for AlGaMnN-H (Figure 4b′). Furthermore, Figure 4(c) indicates one sharp peak around 366.88 cm^{-1} for InGaMnN that has been shifted to several sharp peaks around 640.30, 767.66, 783.92, and 1311.73 cm^{-1} for InGaMnNH (Figure 4c′).

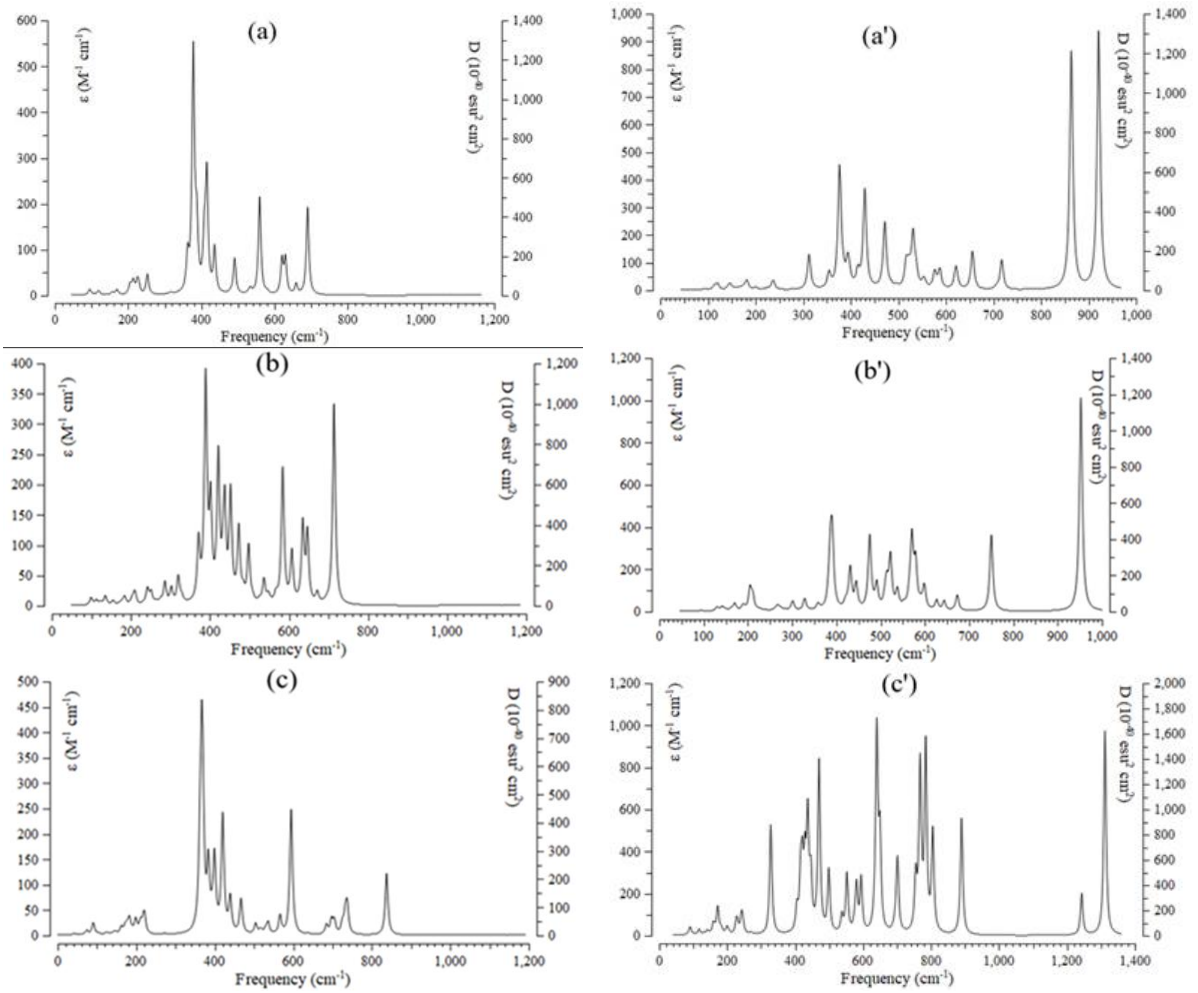

Figure 4. The frequency (cm^{-1}) changes through the IR spectra for heteroclusters of **(a)** GaMnN/GaMnN-H; **(b)** AlGaMnN/AlGaMnN-H; **(c)** InGaMnN/InGaMnN-H.

Energy storage with heteroclusters has been described where the frame of the overcoming cluster is related to GaMnN-H, AlGaMnN-H, and InGaMnN–at high frequency. This property makes these hybrid nanomaterials potentially advantageous for certain high-frequency applications requiring batteries for energy storage. The advantages of manganese over GaN, AlGaN, or InGaN include its higher electron and hole mobility, allowing manganese-doped devices to operate at higher frequencies than non-doped devices. Table 3, through the thermodynamic specifications, concluded that heteroclusters of GaMnN, GaMn–H, AlGaMnN, AlGaMnN-H, InGaMnN, and InGaMnN-H might be a more efficient structure for energy storage in the batteries [66–70].

Table 3. The thermodynamic characters of GaMnN, GaMnN-H, AlGaMnN, AlGaMnN-H, InGaMnN, InGaMnN-H nanoclusters via CAM–B3LYP–D3/6–311+G(d, p) calculation

Compound	Dipole moment (Debye)	$\Delta E^{o}_{ads} \times 10^{-3}$ (kcal/mol)	$\Delta H^{o}_{ads} \times 10^{-3}$ (kcal/mol)	$\Delta G^{o}_{ads} \times 10^{-3}$ (kcal/mol)	$E^{o}_{H-binding}$ (kcal/mol)
GaMnN	4.8247	–383.439	–383.439	–383.483	-
GaMnN–H	7.3741	–383.596	–383.595	–383.636	–157
AlGaMnN	4.7914	–383.095	–383.094	–383.136	-
AlGaMnN–H	7.3741	–383.596	–383.595	–383.636	–501
InGaMnN	7.3629	–383.035	–383.035	–383.082	-
InGaMnN–H	4.3037	–383.472	–383.472	–383.513	–437

Thermodynamic parameters of heteroclusters of GaMnN/GaMnN-H, AlGaMnN/AlGaMnN-H, and InGaMnN/InGaMnN-H have been assigned (Table 3). The changes of Gibbs free energy versus temperature for all nanocomposites could detect the

maximum efficiency of AlGaMnN–H> GaMnN–H> InGaMnN–H for energy storage in the batteries through ΔG_f^o.

The adsorption efficiency of GaMnN-H, AlGaMnN-H, and InGaMnN-H based on dipole moment has been evaluated by the ΔG_f^o. The batteries formed by GaMnN, AlGaMnN, and InGaMnN feature a hierarchical structure with the electron donor/acceptor layer sandwiched by anode and cathode, which raises the importance of controlling the molecular crystal orientation, domain size, and vertical distribution to facilitate the charge collection at electrodes [60–68]. In this paper, we have demonstrated that the nanocomposite semiconductor of gallium nitride-based structure can lead to a significant absorption enhancement in a broad spectral range of incident light in the presence of aluminum, indium, and manganese. A comparison between batteries containing 3d transition metal of Mn-doped GaN, AlGaN, and InGaN shows that a transistor containing these elements shows a more enhanced cell performance than the cells containing only the bare gallium nitride-based structure. This efficient doping strategy not only bridges the gaps of heteroatom-doped GaN-based semiconductor materials but also can provide deep insights into controlling the electrical and optical properties of these doping hybrid nanoclusters.

By using a correlative approach based on spectroscopic techniques, as well as density functional theory calculations, we provided a mechanistic understanding of the chemical transformation that is the origin of the self-improving behavior. A thin layer of bare gallium nitride and its alloys, via a partial manganese substitution at gallium sites, displayed a higher density of catalytic sites for the hydrogen adsorption reaction [71–74].

4. Conclusions

The geometrical parameters of doping manganese on the surface of GaN, AlGaN, and InGaN through the absorption status and current charge density of the batteries were studied. Thermodynamic parameters have constructed a detailed molecular model for atom–atom interactions and a distribution of point charges which can be utilized to reproduce the polarity of the solid material and the adsorbing molecules. Energy storage with heteroclusters has been described, where the frame of the overcoming cluster is related to GaMnN, AlGaMnN, or InGaMnN at high frequencies. This property makes GaMnN, AlGaMnN, or InGaMnN potentially advantageous for certain high-frequency applications requiring batteries for energy storage due to hydrogen adsorption by formation of GaMnN-H, AlGaMnN-H, or InGaMnN-H. The advantages of manganese over GaN, AlGaN, or InGaN include its higher electron and hole mobility, allowing manganese-doped devices to operate at higher frequencies than non-doped devices. Thus, it should be explored for its unique properties, such as its ability to increase energy storage, which could lead to advancements in batteries. Our calculated adsorption energies are in agreement with experimental data for both physisorbed and dissociatively chemisorbed hydrogen on gallium nitride. Furthermore, our calculations show that including dispersion is crucial in order to obtain that level of accuracy for this kind of system.

Author Contributions

Conceptualization, F.M.; methodology, F.M.; data curation, F.M.; formal analysis, F.M.; writing—original draft preparation, F.M.; writing—review and editing, F.M. All authors have read and agreed to the published version of the manuscript.

Institutional Review Board Statement

Not applicable.

Informed Consent Statement

Not applicable.

Data Availability Statement

Not applicable.

Funding

This research received no external funding.

Acknowledgments

In successfully completing this paper and its research, the author is grateful to Kastamonu University.

Conflict of Interest

The author declares no conflict of interest.

References

1. Ma, Y.; Zhang, M.; Wan, S.; Yin, P.; Wang, P.; Cai, D.; Liu, F.; Zheng, Q. Efficient Organic Solar Cells from Molecular Orientation Control of M-Series Acceptors. *Joule* **2021**, *5*, 197-209, https://doi.org/10.1016/j.joule.2020.11.006.
2. Mollaamin, F.; Monajjemi, M. Electric and Magnetic Evaluation of Aluminum–Magnesium Nanoalloy Decorated with Germanium Through Heterocyclic Carbenes Adsorption: A Density Functional Theory Study. *Russ. J. Phys. Chem. B.* **2023**, *17*, 658–672, https://doi.org/10.1134/S1990793123030223.
3. Ma, X.; Zeng, A.; Gao, J.; Hu, Z.; Xu, C.; Son, J.H.; Jeong, S.Y.; Zhang, C.; Li, M.; Wang, K.; Yan, H.; Ma, Z.; Wang, Y.; Woo, H.Y.; Zhang, F. Approaching 18% efficiency of ternary organic photovoltaics with wide bandgap polymer donor and well compatible Y6 : Y6-1O as acceptor. *Natl. Sci. Rev.* **2021**, *8*, nwaa305, https://doi.org/10.1093/nsr/nwaa305.
4. Mollaamin, F.; Monajjemi, M. Nanomaterials for Sustainable Energy in Hydrogen-Fuel Cell: Functionalization and Characterization of Carbon Nano-Semiconductors with Silicon, Germanium, Tin or Lead through Density Functional Theory Study. *Russ. J. Phys. Chem. B.* **2024**, *18*, 607–623, https://doi.org/10.1134/S1990793124020271.
5. Mollaamin, F.; Monajjemi, M. Tailoring and functionalizing the graphitic-like GaN and GaP nanostructures as selective sensors for NO, NO_2, and NH_3 adsorbing: a DFT study. *J. Mol. Model.* **2023**, 29, 170, https://doi.org/10.1007/s00894-023-05567-8.
6. Mollaamin, F.; Mohammadi, S.; Khalaj, Z.; Monajjemi, M. Computational Modelling of Boron Nitride Nanosheet for Detecting and Trapping of Water Contaminant. *Russ. J. Phys. Chem. B.* **2024**, *18*, 67–82, https://doi.org/10.1134/S1990793124010330.
7. Mollaamin, F.; Monajjemi, M. The influence of Sc, V, Cr, Co, Cu, Zn as ferromagnetic semiconductors implanted on B_5N_{10}-nanocarrier for enhancing of NO sensing: An environmental eco-friendly investigation. *Comput. Theor. Chem.* **2024**, *1237*, 114666, https://doi.org/10.1016/j.comptc.2024.114666.
8. Mollaamin, F. Competitive Intracellular Hydrogen-Nanocarrier Among Aluminum, Carbon, or Silicon Implantation: a Novel Technology of Eco-Friendly Energy Storage using Research Density Functional Theory. *Russ. J. Phys. Chem. B.* **2024**, *18*, 805–820, https://doi.org/10.1134/S1990793124700131.

9. Li, X.; Zhou, L.; Lu, X.; Cao, L.; Du, X.; Lin, H.; Zheng, C.; Tao, S. Hydrogen bond induced high-performance quaternary organic solar cells with efficiency up to 17.48% and superior thermal stability. *Mater. Chem. Front.* **2021**, *5*, 3850-3858, https://doi.org/10.1039/D1QM00197C.
10. Lee, K.; Page, R.; Protasenko, V.; Schowalter, L.J.; Toita, M.; Xing, H.G.; Jena, D. MBE growth and donor doping of coherent ultrawide bandgap AlGaN alloy layers on single-crystal AlN substrates. *Appl. Phys. Lett.* **2021**, *118*, 092101, https://doi.org/10.1063/5.0037079.
11. Zhu, C.; Meng, L.; Zhang, J.; Qin, S.; Lai, W.; Qiu, B.; Yuan, J.; Wan, Y.; Huang, W.; Li, Y. A Quinoxaline-Based D–A Copolymer Donor Achieving 17.62% Efficiency of Organic Solar Cells. *Adv. Mater.* **2021**, *33*, 2100474, https://doi.org/10.1002/adma.202100474.
12. Liu, S.; Ye, C.; Cai, X.; Li, S.; Lin, W.; Kang, J. Performance enhancement of AlGaN deep-ultraviolet light-emitting diodes with varied superlattice barrier electron blocking layer. *Appl. Phys. A* **2016**, *122*, 527, https://doi.org/10.1007/s00339-016-0073-0.
13. Li, C.; Zhou, J.; Song, J.; Xu, J.; Zhang, H.; Zhang, X.; Guo, J.; Zhu, L.; Wei, D.; Han, G.; Min, J.; Zhang, Y.; Xie, Z.; Yi, Y.; Yan, H.; Gao, F.; Liu, F.; Sun, Y. Non-fullerene acceptors with branched side chains and improved molecular packing to exceed 18% efficiency in organic solar cells. *Nat. Energy* **2021**, *6*, 605-613, https://doi.org/10.1038/s41560-021-00820-x.
14. Al tahtamouni, T.M.; Lin, J.Y.; Jiang, H.X. Effects of Mg-doped AlN/AlGaN superlattices on properties of p-GaN contact layer and performance of deep ultraviolet light emitting diodes. *AIP Adv.* **2014**, *4*, 047122, https://doi.org/10.1063/1.4871996.
15. Wang, X.; Sun, Q.; Gao, J.; Wang, J.; Xu, C.; Ma, X.; Zhang, F. Recent Progress of Organic Photovoltaics with Efficiency over 17%. *Energies* **2021**, *14*, 4200, https://doi.org/10.3390/en14144200.
16. Sheu, J.-K.; Huang, F.-W.; Lee, C.-H.; Lee, M.-L.; Yeh, Y.-H.; Chen, P.-C.; Lai, W.-C. Improved conversion efficiency of GaN-based solar cells with Mn-doped absorption layer. *Appl. Phys. Lett.* **2013**, *103*, 063906, https://doi.org/10.1063/1.4818340.
17. Xu, C.; Jin, K.; Xiao, Z.; Zhao, Z.; Ma, X.; Wang, X.; Li, J.; Xu, W.; Zhang, S.; Ding, L.; Zhang, F. Wide Bandgap Polymer with Narrow Photon Harvesting in Visible Light Range Enables Efficient Semitransparent Organic Photovoltaics. *Adv. Funct. Mater.* **2021**, *31*, 2107934, https://doi.org/10.1002/adfm.202107934.
18. Hussain, S.; Prodhan, M.T.; Rahman, M.M. Simulation analysis to optimize the performance of homojunction p-i-n $In_{0.7}Ga_{0.3}N$ solar cell. *Semicond. Phys. Quantum Electron. Optoelectron.* **2021**, *24*, 192–199, https://doi.org/10.15407/spqeo24.02.192.
19. Benslim, A.; Meftah, A.; Labed, M.; Meftah, A.; Sengouga, N. Study and optimization of InGaN Schottky solar cell performance. *Optik* **2021**, *247*, 167984, https://doi.org/10.1016/j.ijleo.2021.167984.
20. Jin, K.; Xiao, Z.; Ding, L. D18, an eximious solar polymer!. *J. Semicond.* **2021**, *42*, 010502, https://doi.org/10.1088/1674-4926/42/1/010502.
21. Wang, X.; Sun, Q.; Gao, J.; Wang, J.; Xu, C.; Ma, X.; Zhang, F. Recent Progress of Organic Photovoltaics with Efficiency over 17%. *Energies* **2021**, *14*, 4200, https://doi.org/10.3390/en14144200.
22. Sun, R.; Wang, W.; Yu, H.; Chen, Z.; Xia, X.; Shen, H.; Guo, J.; Shi, M.; Zheng, Y.; Wu, Y.; Yang, W.; Wang, T.; Wu, Q.; Yang, Y.; Lu, X.; Xia, J.; Brabec, C.J.; Yan, H.; Li, Y.; Min, J. Achieving over 17% efficiency of ternary all-polymer solar cells with two well-compatible polymer acceptors. *Joule* **2021**, *5*, 1548-1565, https://doi.org/10.1016/j.joule.2021.04.007.
23. Salem, M.S.; Saif, O.M.; Shaker, A.; Abouelatta, M.; Alzahrani, A.J.; Alanazi, A.; Elsaid, M.K.; Ramadan, R.A. Performance Optimization of the InGaP/GaAs Dual-Junction Solar Cell Using SILVACO TCAD. *Int. J. Photoenergy.* **2021**, *2021*, 8842975, https://doi.org/10.1155/2021/8842975.
24. Neufeld, C.J.; Cruz, S.C.; Farrell, R.M.; Iza, M.; Lang, J.R.; Keller, S.; Nakamura, S.; DenBaars, S.P.; Speck, J.S.; Mishra, U.K. Effect of doping and polarization on carrier collection in InGaN quantum well solar cells. *Appl. Phys. Lett.* **2011**, *98*, 243507, https://doi.org/10.1063/1.3595487.
25. Shah, D.K.; Kc, D.; Kim, T.-G.; Akhtar, M.S.; Kim, C.Y.; Yang, O.B. Influence of minority charge carrier lifetime and concentration on crystalline silicon solar cells based on double antireflection coating: A simulation study. *Opt. Mater.* **2021**, *121*, 111500, https://doi.org/10.1016/j.optmat.2021.111500.
26. Shah, D.K.; Kc, D.; Muddassir, M.; Akhtar, M.S.; Kim, C.Y.; Yang, O.B. A simulation approach for investigating the performances of cadmium telluride solar cells using doping concentrations, carrier lifetimes, thickness of layers, and band gaps. *Sol. Energy* **2021**, *216*, 259-265, https://doi.org/10.1016/j.solener.2020.12.070.

27. Kc, D.; Shah, D.K.; Alanazi, A.M.; Akhtar, M.S. Impact of Different Antireflection Layers on Cadmium Telluride (CdTe) Solar Cells: a PC1D Simulation Study. *J. Electron. Mater.* **2021**, *50*, 2199-2205, https://doi.org/10.1007/s11664-020-08696-5.
28. Gao, Z.; Yang, D.; Sun, C.; Du, L.; Zhang, X.; An, Z. The Corrosion Resistance of Al Film on AZ31 Magnesium Alloys by Magnetron Sputtering. *Metals* **2021**, *11*, 1522, https://doi.org/10.3390/met11101522.
29. Zhang, W.; Zhao, H.; Hu, X.; Ju, D. A Novel Processing for CNT-Reinforced Mg-Matrix Laminated Composites to Enhance the Electromagnetic Shielding Property. *Coatings* **2021**, *11*, 1030, https://doi.org/10.3390/coatings11091030.
30. Bocchetta, P.; Chen, L.-Y.; Tardelli, J.D.C.; Reis, A.C.d.; Almeraya-Calderón, F.; Leo, P. Passive Layers and Corrosion Resistance of Biomedical Ti-6Al-4V and β-Ti Alloys. *Coatings* **2021**, *11*, 487, https://doi.org/10.3390/coatings11050487.
31. Babilas, R.; Spilka, M.; Młynarek, K.; Łoński, W.; Łukowiec, D.; Radoń, A.; Kądziołka-Gaweł, M.; Gębara, P. Glass-Forming Ability and Corrosion Resistance of $Al_{88}Y_{8-x}Fe_{4+x}$ (x = 0, 1, 2 at.%) Alloys. *Materials* **2021**, *14*, 1581, https://doi.org/10.3390/ma14071581.
32. Monajjemi, M.; Khaleghian, M.; Tadayonpour, N.; Mollaamin, F. THE EFFECT OF DIFFERENT SOLVENTS AND TEMPERATURES ON STABILITY OF SINGLE-WALLED CARBON NANOTUBE: A QM/MD STUDY. *Int. J. Nanosci.* **2010**, *09*, 517–529, https://doi.org/10.1142/S0219581X10007071.
33. Bakhshi, K.; Mollaamin, F.; Monajjemi, M. Exchange and Correlation Effect of Hydrogen Chemisorption on Nano V(100) Surface: A DFT Study by Generalized Gradient Approximation (GGA). *J. Comput. Theor. Nanosci.* **2011**, *8*, 763–768, https://doi.org/10.1166/jctn.2011.1750.
34. Mollaamin, F.; Ilkhani, A.; Sakhaei, N.; Bonsakhteh, B.; Faridchehr, A.; Tohidi, S.; Monajjemi, M. Thermodynamic and Solvent Effect on Dynamic Structures of Nano Bilayer-Cell Membrane: Hydrogen Bonding Study. *J. Comput. Theor. Nanosci*. **2015**, *12*, 3148–3154, https://doi.org/10.1166/jctn.2015.4092.
35. Mollaamin, F.; Monajjemi, M. Transition metal (X = Mn, Fe, Co, Ni, Cu, Zn)-doped graphene as gas sensor for CO_2 and NO_2 detection: a molecular modeling framework by DFT perspective. *J. Mol. Model.* **2023**, *29*, 119, https://doi.org/10.1007/s00894-023-05526-3.
36. Mollaamin, F.; Monajjemi, M. Graphene-based resistant sensor decorated with Mn, Co, Cu for nitric oxide detection: Langmuir adsorption & DFT method. *Sens. Rev.* **2023**, *43*, 266–279, https://doi.org/10.1108/sr-03-2023-0040.
37. Lin, J.; Yu, Y.; Xu, Z.; Gao, F.; Zhang, Z.; Zeng, F.; Wang, W.; Li, G. Electronic engineering of transition metal Zn-doped InGaN nanorods arrays for photoelectrochemical water splitting. *J. Power Sources* **2020**, *450*, 227578, https://doi.org/10.1016/j.jpowsour.2019.227578.
38. Kumawat, U.K.; Kumar, K.; Bhardwaj, P.; Dhawan, A. Indium-rich InGaN/GaN solar cells with improved performance due to plasmonic and dielectric nanogratings. *Energy Sci. Eng.* **2019**, *7*, 2469-2482, https://doi.org/10.1002/ese3.436.
39. Mollaamin, F.; Monajjemi M. In Silico-DFT Investigation of Nanocluster Alloys of Al-(Mg, Ge, Sn) Coated by Nitrogen Heterocyclic Carbenes as Corrosion Inhibitors. *J. Clust. Sci.* **2023**, *34*, 2901–2918, https://doi.org/10.1007/s10876-023-02436-5.
40. Zadeh, M.A.A.; Lari, H.; Kharghanian, L.; Balali, E.; Khadivi, R.; Yahyaei, H.; Mollaamin, F.; Monajjemi, M. Density Functional Theory Study and Anti-Cancer Properties of Shyshaq Plant: In View Point of Nano Biotechnology. *J. Comput. Theor. Nanosci.* **2015**, *12*, 4358-4367, https://doi.org/10.1166/jctn.2015.4366.
41. Mollaamin, F.; Shahriari, S.; Monajjemi, M.; Khalaj, Z. Nanocluster of Aluminum Lattice via Organic Inhibitors Coating: A Study of Freundlich Adsorption. *J. Clust. Sci.* **2023**, *34*, 1547-1562, https://doi.org/10.1007/s10876-022-02335-1.
42. Sarasia, E.M.; Afsharnezhad, S.; Honarparvar, B.; Mollaamin, F.; Monajjemi, M. Theoretical study of solvent effect on NMR shielding tensors of luciferin derivatives. *Phys. Chem. Liq.* **2011**, *49*, 561-571, https://doi.org/10.1080/00319101003698992.
43. Mollaamin, F.; Monajjemi, M. Molecular modelling framework of metal-organic clusters for conserving surfaces: Langmuir sorption through the TD-DFT/ONIOM approach. *Mol. Simul.* **2023**, *49*, 365–376, https://doi.org/10.1080/08927022.2022.2159996.
44. Mollaamin, F.; Monajjemi, M. Selectivity and Sensitivity Evaluation of Embedded BN-Nanostructure as a Gas Detector for Air Pollution Scavenging: a Theoretical Study. *Russ. J. Phys. Chem. B* **2024**, *18*, 1177–1198, https://doi.org/10.1134/S1990793124700507.

45. Monajjemi, M.; Noei, M.; Mollaamin, F. Design of fMet-tRNA and Calculation of its Bonding Properties by Quantum Mechanics. *Nucleos. Nucleot. Nucleic Acids* **2010**, *29*, 676–683, https://doi.org/10.1080/15257771003781642.
46. Mollaamin, F.; Monajjemi, M. Effect of Implanted Titanium, Vanadium or Chromium on Boron Nitride Surface for Increasing Carbon Monoxide Adsorption: Designing Gas Sensor for Green Chemistry Future. *Russ. J. Phys. Chem. B* **2024**, *18*, 1199–1216, https://doi.org/10.1134/S1990793124700519.
47. Monajjemi, M.; Karachi, N.; Mollaamin, F. The Investigation of Sequence-dependent Interaction of Messenger RNA Binding to Carbon Nanotube. *Fuller. Nanotub. Carbon Nanostructures* **2014**, *22*, 643–662, https://doi.org/10.1080/1536383X.2012.717557.
48. Mollaamin, F. Investigating the Treatment of Transition Metals for Ameliorating the Ability of Boron Nitride for Gas Sensing & Removing: A Molecular Characterization by DFT Framework. *Prot. Met. Phys. Chem. Surf.* **2024**, *60*,1050–1063, https://doi.org/10.1134/S2070205124702502.
49. Khalili Hadad, B.; Mollaamin, F.; Monajjemi, M. Biophysical chemistry of macrocycles for drug delivery: a theoretical study. *Russ. Chem. Bull*. **2011**, *60*, 238–241, https://doi.org/10.1007/s11172-011-0039-5.
50. Monajjemi, M.; Yamola, H.; Mollaamin, F. Study of Bio-nano Interaction Outlook of Amino Acids on Single-walled Carbon Nanotubes. *Fuller. Nanotub. Carbon Nanostructures* **2014**, *22*, 595–603, https://doi.org/10.1080/1536383X.2012.702163.
51. Mollaamin, F.; Monajjemi, M. Adsorption ability of Ga_5N_{10} nanomaterial for removing metal ions contamination from drinking water by DFT. *Int. J. Quantum Chem.* **2024**, *124*, e27348, https://doi.org/10.1002/qua.27348.
52. Mollaamin, F. Alkali Metals Doped on Tin-Silicon and Germanium-Silicon Oxides for Energy Storage in Hybrid Biofuel Cells: A First-Principles Study. *Russ. J. Phys. Chem. B.* **2025**, *19*, 720–734.
53. Frisch, M.J.; Trucks, G.W.; Schlegel, H.B.; Scuseria, G.E.; Robb, M.A.; Cheeseman, J.R.; Scalmani, G.; Barone, V.; Petersson, G.A.; Nakatsuji, H.; Li, X.; Caricato, M.; Marenich, A.V.; Bloino, J.; Janesko, B.G.; Gomperts, R.; Mennucci, B.; Hratchian, H.P.; Ortiz, J. V.; Izmaylov, A. F.; Sonnenberg, J.L.; Williams-Young, D.; Ding, F.; Lipparini, F.; Egidi, F.; Goings, J.; Peng, B.; Petrone, A.; Henderson, T.; Ranasinghe, D.; Zakrzewski, V.G.; Gao, J.; Rega, N.; Zheng, G.; Liang, W.; Hada, M.; Ehara, M.; Toyota, K.; Fukuda, R.; Hasegawa, J.; Ishida, M.; Nakajima, T.; Honda, Y.; Kitao, O.; Nakai, H.; Vreven, T.; Throssell, K.; Montgomery, J.A., Jr.; Peralta, J.E.; Ogliaro, F.; Bearpark, M.J.; Heyd, J.J.; Brothers, E.N.; Kudin, K.N.; Staroverov, V.N.; Keith, T.A.; Kobayashi, R.; Normand, J.; Raghavachari, K.; Rendell, A.P.; Burant, J.C.; Iyengar, S.S.; Tomasi, J.; Cossi, M.; Millam, J.M.; Klene, M.; Adamo, C.; Cammi, R.; Ochterski, J.W.; Martin, R.L.; Morokuma, K.; Farkas, O.; Foresman, J.B.; Fox, D.J. Gaussian 16, Revision C.01, Gaussian, Inc., Wallingford CT, **2016**.
54. Dennington, R.; Keith, T.A.; Millam, J.M. GaussView 6.06.16. Semichem Inc., Shawnee Mission: **2016**.
55. Mollaamin, F.; Shahriari, S.; Monajjemi, M. Influence of Transition Metals for Emergence of Energy Storage in Fuel Cells through Hydrogen Adsorption on the MgAl Surface. *Russ. J. Phys. Chem. B* **2024**, *18*, 398–418, https://doi.org/10.1134/S199079312402026X.
56. Shahriari, S.; Mollaamin, F.; Monajjemi, M. Increasing the Performance of {[(1-x-y) $LiCo_{0.3}Cu_{0.7}$] (Al and Mg doped)] O_2}, xLi_2MnO_3, $yLiCoO_2$ Composites as Cathode Material in Lithium-Ion Battery: Synthesis and Characterization. *Micromachines* **2023**, *14*, 241, https://doi.org/10.3390/mi14020241.
57. Mollaamin, F.; Monajjemi, M. Boron nitride doped with transition metals for carbon monoxide detection: a promising nanosensor for air cleaning. *Sens. Rev.* **2024**, *44*, 179–193, https://doi.org/10.1108/SR-01-2024-0066.
58. Mollaamin, F.; Monajjemi, M. Fractal Dimension on Carbon Nanotube-Polymer Composite Materials Using Percolation Theory. *J. Comput. Theor. Nanosci.* **2012**, *9*, 597–601, https://doi.org/10.1166/jctn.2012.2067.
59. Mollaamin, F.; Monajjemi, M. In Situ Ti-Embedded SiC as Chemiresistive Nanosensor for Safety Monitoring of CO, CO_2, NO, NO_2: Molecular Modelling by Conceptual Density Functional Theory. *Russ. J. Phys. Chem. B.* **2024**, *18*, 49–66. https://doi.org/10.1134/S1990793124010159.
60. Mollaamin, F.; Monajjemi, M. Trapping of toxic heavy metals from water by GN–nanocage: Application of nanomaterials for contaminant removal technique. *J. Mol. Struct.* **2024**, *1300*, 137214, https://doi.org/10.1016/j.molstruc.2023.137214.
61. Trontelj, Z.; Pirnat, J.; Jazbinšek, V.; Lužnik, J.; Srčič, S.; Lavrič, Z.; Beguš, S.; Apih, T.; Žagar, V.; Seliger, J. Nuclear Quadrupole Resonance (NQR)—A Useful Spectroscopic Tool in Pharmacy for the Study of Polymorphism. *Crystals* **2020**, *10*, 450, https://doi.org/10.3390/cryst10060450.

62. Sciotto, R.; Ruiz Alvarado, I.A.; Schmidt, W.G. Substrate Doping and Defect Influence on P-Rich InP(001):H Surface Properties. *Surfaces* **2024**, *7*, 79-87, https://doi.org/10.3390/surfaces7010006.
63. Luo, J.; Wang, C.; Wang, Z.; Guo, Q.; Yang, J.; Zhou, R.; Matano, K.; Oguchi, T.; Ren, Z.; Cao, G.; Zheng, G.-Q. NMR and NQR studies on transition-metal arsenide superconductors $LaRu_2As_2$, $KCa_2Fe_4As_4F_2$, and $A_2Cr_3As_3$*. *Chinese Phys. B* **2020**, *29*, 067402, https://doi.org/10.1088/1674-1056/ab892d.
64. Hotra, O.; Samila, A. A Low-Cost Digital Pulsed Coherent Spectrometer for Investigation of NQR in Layered Semiconductor GaSe and InSe Crystals. *Electronics* **2020**, *9*, 1996, https://doi.org/10.3390/electronics9121996.
65. Mollaamin, F.; Monajjemi, M. Structural, Electromagnetic and Thermodynamic Analysis of Ion Pollutants Adsorption in Water by Gallium Nitride Nanomaterial: a Green Chemistry Application. *Russ. J. Phys. Chem. B.* **2024**, *18*, 533–548, https://doi.org/10.1134/S199079312402012X.
66. Li, Y.; Chen, H.; Zhang, J. Carrier Blocking Layer Materials and Application in Organic Photodetectors. *Nanomaterials* **2021**, *11*, 1404, https://doi.org/10.3390/nano11061404.
67. Yuan, J.; Yuan, H.; Huang, S.; Liu, L.; Fu, F.; Zhang, Y.; Cheng, F.; Li, J. Comprehensive performance, bacterial community structure of single-chamber microbial fuel cell affected by COD/N ratio and physiological stratifications in cathode biofilm. *Bioresour. Technol.* **2021**, *320*, 124416, https://doi.org/10.1016/j.biortech.2020.124416.
68. Park, Y.; Yu, J.; Nguyen, V.K.; Park, S.; Kim, J.; Lee, T. Understanding complete ammonium removal mechanism in single-chamber microbial fuel cells based on microbial ecology. *Sci. Total Environ.* **2021**, *764*, 144231, https://doi.org/10.1016/j.scitotenv.2020.144231.
69. Deng, L.; Ren, Y.; Wei, C.; Wang, J. Biodegradation of pyrene by a novel strain of *Castellaniella* sp. under denitrifying condition. *J. Environ. Chem. Eng.* **2021**, *9*, 104970, https://doi.org/10.1016/j.jece.2020.104970.
70. Taşkan, B.; Taşkan, E. Inhibition of AHL-mediated quorum sensing to control biofilm thickness in microbial fuel cell by using *Rhodococcus sp.* BH4. *Chemosphere* **2021**, *285*, 131538, https://doi.org/10.1016/j.chemosphere.2021.131538.
71. Li, Y.; Huang, X.; Ding, K.; Sheriff, H.K.M.; Ye, L.; Liu, H.; Li, C.-Z.; Ade, H.; Forrest, S.R. Non-fullerene acceptor organic photovoltaics with intrinsic operational lifetimes over 30 years. *Nat. Commun.* **2021**, *12*, 5419, https://doi.org/10.1038/s41467-021-25718-w.
72. Mollaamin, F.; Baei, M.T.; Monajjemi, M.; Zhiani, R.; Honarparvar, B. A DFT study of hydrogen chemisorption on V (100) surfaces. *Russ. J. Phys. Chem.* **2008**, *82*, 2354-2361, https://doi.org/10.1134/S0036024408130323.
73. Bernardo, G.; Lopes, T.; Lidzey, D.G.; Mendes, A. Progress in Upscaling Organic Photovoltaic Devices. *Adv. Energy Mater.* **2021**, *11*, 2100342, https://doi.org/10.1002/aenm.202100342.
74. Wang, X.; Sun, Q.; Gao, J.; Ma, X.; Son, J.H.; Jeong, S.Y.; Hu, Z.; Niu, L.; Woo, H.Y.; Zhang, J.; Zhang, F. Ternary Organic Photovoltaic Cells Exhibiting 17.59% Efficiency with Two Compatible Y6 Derivations as Acceptor. *Solar RRL* **2021**, *5*, 2100007, https://doi.org/10.1002/solr.202100007.

Publisher's Note & Disclaimer